# UWB Localization Strategies for Autonomous Transport Vehicle Docking Operations

Markus Pichler-Scheder*, Richard Schmidt†, and Florian Hammer‡
Linz Center of Mechatronics GmbH
Altenberger Str. 69, 4040 Linz, Austria
Email: *markus.pichler-scheder@lcm.at, †richard.schmidt@lcm.at, ‡florian.hammer@lcm.at

***Abstract*—Autonomous transport vehicles require robust solutions to operate seamlessly across diverse weather conditions. The EU-funded AWARD project (H2020) addresses this imperative by presenting a hub-to-hub material transport solution. However, traditional satellite-based navigation (GNSS) encounters limitations in severe weather and does not work well without line-of-sight satellite connection. To enhance vehicle position data acquisition at docking ramps, a stationary Ultra-Wideband (UWB) localization system has been implemented. Our algorithmic approach explores four methods for estimating the vehicle's 2D-pose, encompassing position and orientation, based on an Extended Kalman Filter (EKF) for simultaneous estimation of synchronization and localization states. Our measurement results demonstrate that geometrically interlocking the tags and incorporating a vehicle motion model into the localization algorithm significantly enhance estimation accuracy.**

## I. Introduction

The era of autonomous transport is upon us, ushering in a transformative paradigm where vehicles navigate and operate without human intervention. This cutting-edge frontier in transportation promises increased efficiency, enhanced safety, and a revolutionary shift in the dynamics of mobility.

The EU project AWARD H2020 ("All Weather Autonomous Real logistics operations and Demonstrations", [1]) aimed at the roll-out of driverless transportation. The objective was to implement a secure and efficient heavy-duty transportation system for real-life logistics, capable of operating seamlessly in all weather conditions. The project was focused on four individual use cases: Forklift transportation in a warehouse, transport of goods on an airport, container transport and automated boat loading in a port, and hub-to-hub shuttle service from a production site to a logistics hub. In hub-to-hub scenarios, conventional sensor equipment for autonomous driving may face challenges in severe weather conditions like heavy rain or fog. Also, when the vehicle is (partly) under a roof and does not have line-of-sight satellite connection, GNSS accuracy may degrade. Especially in docking scenarios, supplementing with a radio-based localization system can offer additional safety.

Ultra-wideband technology (UWB, [2], [3]) provides infrastructure-based position estimation of mobile tags within a region bounded by a number of connected anchor nodes of known position. UWB-localization accuracy typically lies in the range of centimeters to tens of centimeters. Localization of mobile tags is accomplished by continuous radio communication between tags and anchors and using measurements of transmission and reception time stamps (time-of-arrival, ToA) of exchanged data packets for estimation. Since clocks are local to the individual anchors and tags and there is no hardware synchronization, clock parameters must be estimated along with the mobile tag locations. For this purpose, simultaneous localization and synchronization algorithms [4]–[7] have been developed.

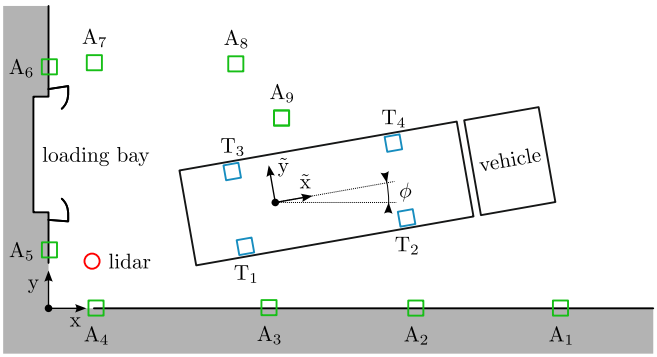


Fig. 1. Top view of UWB anchor and tag setup with coordinate systems. Vehicle origin is the center point between the (unsteered) back wheels.

In the proposed system, the positions of the tags and the vehicle to be localized as well as clock parameters are estimated using an Extended Kalman Filter (EKF) based on an underlying state model. While this is a common choice in localization [8], our approach does not require a specific packet exchange schedule and relies solely on broadcast messages. This greatly simplifies deployment and computation while simultaneously providing accuracy achievable by round-trip time of flight measurement (RToF). Furthermore, we use tag to tag communication and geometric constraints to significantly improve estimation results.

In this paper, we first illustrate the measurement setting and the UWB system setup in Section II. We then describe our localization algorithm in Section III. In Section IV, we present and discuss the results of our measurements. Finally, we conclude our paper in Section V.

## II. Measurement Setup

The UWB localization system has been installed at a docking ramp on the premises of AWARD project partner DB Schenker in Gunskirchen, Austria. It is based on Qorvo DW1000 UWB hardware [9] and consists of anchor stations

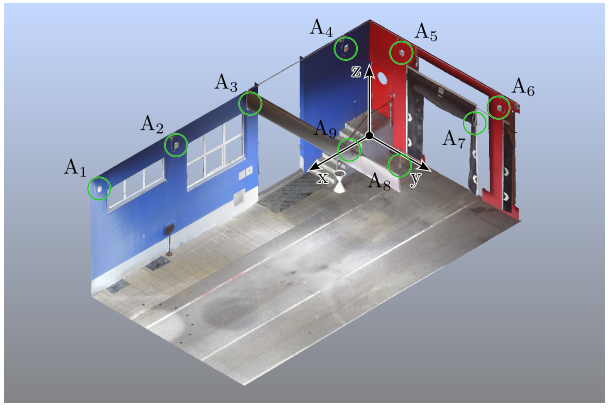


Fig. 2. Setup of anchor stations in loading dock.

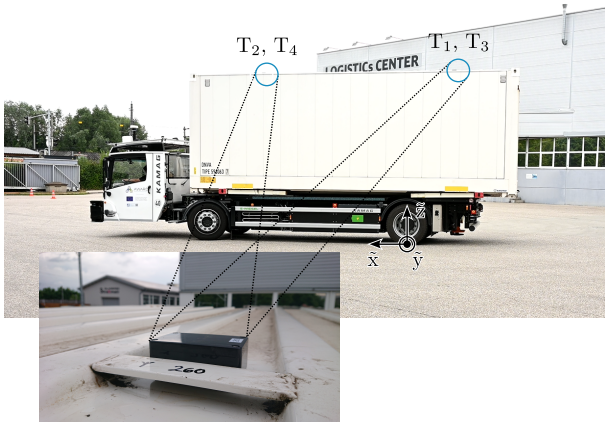


Fig. 3. Vehicle with tags mounted on top.

connected to a measurement PC via Power-over-Ethernet (PoE). As shown in Figs. 1 and 2, a total number of $K_\mathrm{A} = 9$ anchors have been placed at fixed and known positions on the walls of the hub building. Encased in weather-proof housing, $K_\mathrm{T} = 4$ mobile tags have been mounted in a fixed rectangular arrangement via magnets directly onto the metallic transportation container carried by an autonomous transport vehicle, as illustrated in Fig. 3. In the following, we will refer to anchors and tags as units where no distinction is necessary.

As shown in Fig. 4, each unit transmits packets as broadcasts with a slightly jittered repetition rate, and switches to receive mode to listen for packets from other units when it is not transmitting itself. This may lead to collisions and therefore packet loss but requires no scheduling protocol, which greatly simplifies deployment. In this application and with the chosen configuration, the connectivity has been found to be sufficient nonetheless. Each transmitted packet contains the transmitter ID and an ascending packet number as well as the time of transmission as measured in the local transmitter clock. Upon reception by another unit, the time of arrival is estimated in receiver clock time and added to the packet, along with receiver ID. When a packet is received by an anchor, the associated data is subsequently transferred to the measurement

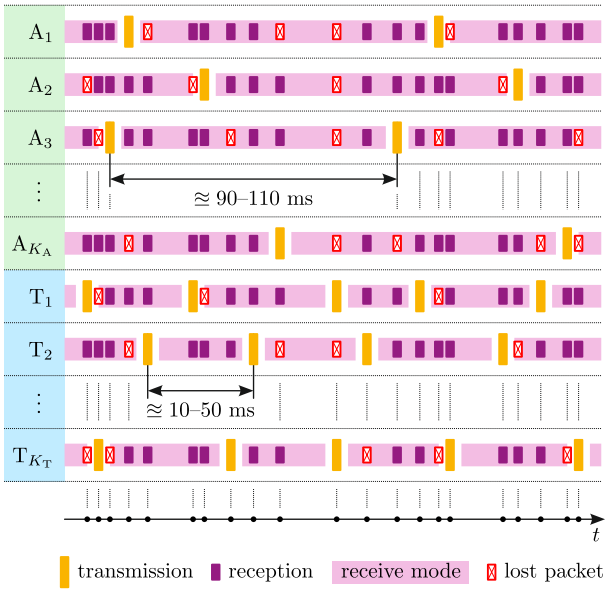


Fig. 4. Exemplary timing of transmissions and receptions from/to anchors and tags. Units are in receive mode when not transmitting, with some time for switching between modes. Packet loss occurs e.g. due to collisions, obstacles in the propagation path, or if the maximum measurement range is exceeded.

PC via Ethernet. To enable two-way measurements between all units, wireless tags collect all received packets including associated timestamps and transmit the contained information as user data with their next transmission.

A 2D lidar system (SLAMTEC RPLIDAR C1 [10]) has been positioned at the ramp and connected to the Measurement PC. A continuous least squares fit of the container profile to the measured point cloud provides vehicle pose ground truth data for estimation error evaluation.

## III. Localization Algorithm

The localization algorithm is based on an EKF for simultaneous estimation of synchronization and localization states. It also allows the pose estimation of rigid bodies on which tags are mounted, so that fixed relative tag positions and a vehicle motion model can be incorporated. Due to the asynchronous communications protocol, there is no fixed discretization interval in time. Instead, each packet is processed immediately after it is received. The algorithm keeps an ordered backlog of packets for a certain time so that out of sequence arrivals lead to a reprocessing and update of the latest estimates.

In this work we will compare the results of vehicle pose estimation using four different configurations (C1–C4):

- C1: tags are free-floating;
  tags only communicate with anchors, not with other tags
- C2: tags are free-floating;
  tags communicate with anchors and other tags
- C3: tags have a rigid connection to the vehicle;
  tags communicate with anchors and other tags
- C4: tags have a rigid connection to the vehicle that moves using a simple vehicle model;
  tags communicate with anchors and other tags

While a detailed description of the algorithm is out of scope of this work and is planned to be published in a subsequent article, we will give a brief summary of the main points.

### A. Indices

We will denote the index of receptions in order of arrival at the localization algorithm by $n$ (cf. Fig. 4). This is the order of processing and therefore the time index of the EKF. The transmitting (tx) and receiving (rx) units for packet $n$ are $k_{\mathrm{t},n}$ and $k_{\mathrm{r},n}$, respectively. Furthermore, the unit-specific index of tx or rx by each of these units at time $n$ is denoted by $m_n^k$, and the total transmission index for reception $n$ is $m_n$. For brevity we will use the abbreviations

$$k_\mathrm{t} \equiv k_{\mathrm{t},n} \qquad k_\mathrm{r} \equiv k_{\mathrm{r},n}$$
$$m_\mathrm{t} \equiv m_n^{k_\mathrm{t}} \qquad m_\mathrm{r} \equiv m_n^{k_\mathrm{r}}.$$

### B. Input and state vectors

In our EKF implementation, we propagate states using the time that has elapsed since the previous transmission or reception (trx) as input $\mathbf{u}_{\mathrm{k},n}$. Measured in local time of each unit (denoted by $\tilde{\cdot}$), we get the time differences for the tx $\Delta\tilde{t}_n^{k_\mathrm{t}}$ and the rx units $\Delta\tilde{t}_n^{k_\mathrm{r}}$ between the current and the previous packet from/to that unit

$$\mathbf{u}_{\mathrm{k},n} \equiv \begin{bmatrix}\Delta\tilde{t}_n^{k_\mathrm{t}} \\ \Delta\tilde{t}_n^{k_\mathrm{r}}\end{bmatrix} = \begin{bmatrix}\tilde{t}_{m_\mathrm{t}}^{k_\mathrm{t}} - \tilde{t}_{m_\mathrm{t}-1}^{k_\mathrm{t}} \\ \tilde{t}_{m_\mathrm{r}}^{k_\mathrm{r}} - \tilde{t}_{m_\mathrm{r}-1}^{k_\mathrm{r}}\end{bmatrix},$$

where $\tilde{t}_m^k$ is the local clock measurement of the $m$th tx or rx of unit $k$. Note that for transmissions received by more than one unit, $\Delta\tilde{t}_n^{k_\mathrm{t}}$ becomes zero starting from the second reception. In C1 and C2, the total input vector $\mathbf{u}_n = \mathbf{u}_{\mathrm{k},n}$; in C3 and C4, $\mathbf{u}_n = \begin{bmatrix}\mathbf{u}_{\mathrm{k},n} & u_{\mathrm{t},n}\end{bmatrix}^\mathrm{T}$, where $u_{\mathrm{t},n}$ will be defined in (1).

The unit state vector $\mathbf{x}_{\mathrm{k},n} = \begin{bmatrix}\mathbf{x}_n^{k\in\mathcal{K}_\mathrm{A}} & \mathbf{x}_n^{k\in\mathcal{K}_\mathrm{T}}\end{bmatrix}^\mathrm{T}$ consists of the assembled state vectors of all units $k \in \mathcal{K} = \mathcal{K}_\mathrm{A} \cup \mathcal{K}_\mathrm{T}$, where $\mathcal{K}_\mathrm{A}$ and $\mathcal{K}_\mathrm{T}$ are the index sets of all anchors and tags, respectively. For anchors of known location, only synchronization states $\mathbf{x}_{\mathrm{s},n}^k$ must be estimated to account for unsynchronized clocks, therefore $\mathbf{x}_n^{k\in\mathcal{K}_\mathrm{A}} = \mathbf{x}_{\mathrm{s},n}^k$. In C1 and C2, synchronization and location states $\mathbf{x}_{\mathrm{l},n}^k$ are estimated for individual mobile tags, i.e. $\mathbf{x}_n^{k\in\mathcal{K}_\mathrm{T}} = \begin{bmatrix}\mathbf{x}_{\mathrm{s},n}^k & \mathbf{x}_{\mathrm{l},n}^k\end{bmatrix}^\mathrm{T}$, and the total state vector becomes $\mathbf{x}_n = \mathbf{x}_{\mathrm{k},n}$. In C3 and C4, pose $\mathbf{x}_{\mathrm{l},n}$ is estimated for the vehicle instead of individual tags, which makes $\mathbf{x}_n^{k\in\mathcal{K}_\mathrm{T}} = \mathbf{x}_{\mathrm{s},n}^k$ and $\mathbf{x}_n = \begin{bmatrix}\mathbf{x}_{\mathrm{l},n} & \mathbf{x}_{\mathrm{k},n}\end{bmatrix}^\mathrm{T}$.

In the prediction step, only states of the current packet's tx and rx units $k_\mathrm{t}$ and $k_\mathrm{r}$ are considered, while the others remain unchanged. This allows for a particularly efficient computation. Consequently, the state vector $\mathbf{x}_n^k$ for each unit represents the time of the last trx from that unit and is not synchronous for all units. We therefore only actually output unit states whenever this unit has a current trx. For tx with multiple rx, state output occurs only after the last rx has been received, which is the most informed estimate at this time.

The state transition equations for the vehicle and units $k \in \{k_\mathrm{t}, k_\mathrm{r}\}$ are given below. As stated above, for $k \neq \{k_\mathrm{t}, k_\mathrm{r}\}$ we have $\mathbf{x}_n^k \equiv \mathbf{f}^k(\mathbf{x}_{n-1}) = \mathbf{x}_{n-1}^k$.

### C. Synchronization state transition

For synchronization, we use an affine clock model in which we denote the current time at unit $k$ by $t_n^k$, and the clock skew by $\tau_n^k$. The state transition equation is

$$\mathbf{x}_{\mathrm{s},n}^k \equiv \begin{bmatrix}t_n^k \\ \tau_n^k\end{bmatrix} = \underbrace{\begin{bmatrix}t_{n-1}^k + \left(1+\tau_{n-1}^k\right)\Delta\tilde{t}_n^k \\ \tau_{n-1}^k\end{bmatrix}}_{\mathbf{f}_\mathrm{s}^k(\mathbf{x}_{n-1},\mathbf{u}_n)} + \underbrace{\begin{bmatrix}\delta t_n^k \\ \delta\tau_n^k\end{bmatrix}}_{\mathbf{w}_{\mathrm{s},n}^k}$$

with clock drift modeled as a zero-mean multivariate normal distribution with covariance matrix $\mathbf{Q}_{\mathrm{s},n}^k$,

$$\mathbf{w}_{\mathrm{s},n}^k \sim \mathcal{N}\left(\mathbf{0}, \mathbf{Q}_{\mathrm{s},n}^k\right) \quad \mathbf{Q}_{\mathrm{s},n}^k = \begin{bmatrix}\frac{1}{3}(\Delta\tilde{t}_n^k)^3 & \frac{1}{2}(\Delta\tilde{t}_n^k)^2 \\ \frac{1}{2}(\Delta\tilde{t}_n^k)^2 & \Delta\tilde{t}_n^k\end{bmatrix}\sigma_\tau^2.$$

Here, we assume that $\delta\tau_n^k$ follows a Wiener process so that the variance of $\tau$ increases linearly in time with rate $\sigma_\tau^2$.

### D. Location state transition

*1) Configurations C1 and C2:* Locations are estimated for individual tags, their mounting on a rigid body is disregarded. The difference between C1 and C2 is that in C1, packets with mobile tags as transmitter and receiver are discarded before evaluation. For location we use the constant velocity model

$$\mathbf{x}_{\mathrm{l},n}^k \equiv \begin{bmatrix}\bar{\mathbf{p}}_n^k \\ \bar{\mathbf{v}}_n^k\end{bmatrix} = \underbrace{\begin{bmatrix}\bar{\mathbf{p}}_{n-1}^k + \bar{\mathbf{v}}_{n-1}^k\,\Delta\tilde{t}_n^k \\ \bar{\mathbf{v}}_{n-1}^k\end{bmatrix}}_{\mathbf{f}_\mathrm{l}^k(\mathbf{x}_{n-1},\mathbf{u}_n)} + \underbrace{\begin{bmatrix}\boldsymbol{\delta}\bar{\mathbf{p}}_n^k \\ \boldsymbol{\delta}\bar{\mathbf{v}}_n^k\end{bmatrix}}_{\mathbf{w}_{\mathrm{l},n}^k}$$

with plane position $\bar{\mathbf{p}}_n^k = \begin{bmatrix}p_{\mathrm{x},n}^k & p_{\mathrm{y},n}^k\end{bmatrix}^\mathrm{T}$, velocity $\bar{\mathbf{v}}_n^k = \begin{bmatrix}v_{\mathrm{x},n}^k & v_{\mathrm{y},n}^k\end{bmatrix}^\mathrm{T}$, and position $\mathbf{p}_n^k = \begin{bmatrix}\bar{\mathbf{p}}_n^k & p_\mathrm{z}^k\end{bmatrix}^\mathrm{T}$ in space with constant $p_\mathrm{z}^k$. Position and velocity variation $\boldsymbol{\delta}\bar{\mathbf{p}}_n^k = \begin{bmatrix}\delta p_{\mathrm{x},n}^k & \delta p_{\mathrm{y},n}^k\end{bmatrix}^\mathrm{T}$ and $\boldsymbol{\delta}\bar{\mathbf{v}}_n^k = \begin{bmatrix}\delta v_{\mathrm{x},n}^k & \delta v_{\mathrm{y},n}^k\end{bmatrix}^\mathrm{T}$ are distributed according to a zero-mean multivariate normal distribution with covariance matrix $\mathbf{Q}_{\mathrm{l},n}^k$,

$$\mathbf{w}_{\mathrm{l},n}^k \sim \mathcal{N}\left(\mathbf{0}, \mathbf{Q}_{\mathrm{l},n}^k\right) \quad \mathbf{Q}_{\mathrm{l},n}^k = \begin{bmatrix}\mathbf{I}\frac{1}{3}(\Delta\tilde{t}_n^k)^3 & \mathbf{I}\frac{1}{2}(\Delta\tilde{t}_n^k)^2 \\ \mathbf{I}\frac{1}{2}(\Delta\tilde{t}_n^k)^2 & \mathbf{I}\Delta\tilde{t}_n^k\end{bmatrix}\sigma_\mathrm{v}^2,$$

since $\delta v_{\mathrm{x},n}^k$ and $\delta v_{\mathrm{y},n}^k$ are modeled as independent Wiener processes with variance rate $\sigma_\mathrm{v}^2$. $\mathbf{I}$ denotes the identity matrix.

*2) Configurations C3 and C4:* In configurations C3 and C4, the vehicle pose—given by the position of the back wheel center in the plane $\bar{\mathbf{p}}_n = \begin{bmatrix}p_{\mathrm{x},n} & p_{\mathrm{y},n}\end{bmatrix}^\mathrm{T}$ and angle about the z-axis $\phi_n$ (cf. Fig. 1)—as well as velocity $\bar{\mathbf{v}}_n = \begin{bmatrix}v_{\mathrm{x},n} & v_{\mathrm{y},n}\end{bmatrix}^\mathrm{T}$ is estimated while considering the relative tag mounting positions $\tilde{\bar{\mathbf{p}}}^k = \begin{bmatrix}\tilde{p}_\mathrm{x}^k & \tilde{p}_\mathrm{y}^k\end{bmatrix}^\mathrm{T}$ on the vehicle. Individual tag locations are calculated as $\mathbf{p}_n^k = \begin{bmatrix}\bar{\mathbf{p}}_n^k & p_\mathrm{z}^k\end{bmatrix}^\mathrm{T}$ with constant $p_\mathrm{z}^k$ and

$$\bar{\mathbf{p}}_n^k = \bar{\mathbf{p}}_n + \begin{bmatrix}\cos(\phi_n) & -\sin(\phi_n) \\ \sin(\phi_n) & \cos(\phi_n)\end{bmatrix}\tilde{\bar{\mathbf{p}}}^k.$$

For pose propagation in these configurations we also require the elapsed time since the last transmission, which is

$$u_{\mathrm{t},n} \equiv \Delta t_{\mathrm{t},n} = \Delta\tilde{t}_n^{k_\mathrm{t}} + t_{n-1}^{k_\mathrm{t}} - t_{n-1}^{k_{\mathrm{t},n-1}}. \tag{1}$$

Note that for pose propagation we do not strictly separate local and estimated time intervals, but since $\tau_n^k \ll 1$, this leads to negligible error.

*3) Configuration C3:* In C3, the vehicle can move in all directions in the plane, its motion equations are therefore given as

$$\mathbf{x}_{\mathrm{l},n} \equiv \begin{bmatrix} \bar{\mathbf{p}}_n \\ \bar{\mathbf{v}}_n \\ \phi_n \end{bmatrix} = \underbrace{\begin{bmatrix} \bar{\mathbf{p}}_{n-1} + \bar{\mathbf{v}}_{n-1}\Delta t_{\mathrm{t},n} \\ \bar{\mathbf{v}}_{n-1} \\ \phi_{n-1} \end{bmatrix}}_{\mathbf{f}_\mathrm{l}(\mathbf{x}_{n-1},\mathbf{u}_n)} + \underbrace{\begin{bmatrix} \boldsymbol{\delta}\bar{\mathbf{p}}_n \\ \boldsymbol{\delta}\bar{\mathbf{v}}_n \\ \delta\phi_n \end{bmatrix}}_{\mathbf{w}_{\mathrm{l},n}},$$

Vehicle position $\boldsymbol{\delta}\bar{\mathbf{p}}_n = \begin{bmatrix}\delta\bar{p}_{\mathrm{x},n} & \delta\bar{p}_{\mathrm{y},n}\end{bmatrix}^\mathrm{T}$, velocity $\boldsymbol{\delta}\bar{\mathbf{v}}_n = \begin{bmatrix}\delta\bar{v}_{\mathrm{x},n} & \delta\bar{v}_{\mathrm{y},n}\end{bmatrix}^\mathrm{T}$, and angle variation $\delta\phi_n$ are distributed as

$$\mathbf{w}_{\mathrm{l},n} \sim \mathcal{N}(\mathbf{0}, \mathbf{Q}_{\mathrm{l},n}) \qquad \mathbf{Q}_{\mathrm{l},n} = \begin{bmatrix} \mathbf{Q}_{\mathrm{pv},n} & \mathbf{0} \\ \mathbf{0} & \Delta t_{\mathrm{t},n}\sigma_\phi^2 \end{bmatrix}$$
$$\mathbf{Q}_{\mathrm{pv},n} = \begin{bmatrix} \mathbf{I}\frac{1}{3}(\Delta t_{\mathrm{t},n})^3 & \mathbf{I}\frac{1}{2}(\Delta t_{\mathrm{t},n})^2 \\ \mathbf{I}\frac{1}{2}(\Delta t_{\mathrm{t},n})^2 & \mathbf{I}\Delta t_{\mathrm{t},n} \end{bmatrix}\sigma_\mathrm{v}^2$$

where $\sigma_\mathrm{v}^2$ and $\sigma_\phi^2$ are the velocity and angle variation rate of independent Wiener processes, respectively.

*4) Configuration C4:* Vehicle motion is restricted so that it only moves in wheel direction, i.e. there is no sideways motion allowed. We therefore only have scalar velocity in vehicle x-direction and the state transition becomes

$$\mathbf{x}_{\mathrm{l},n} = \begin{bmatrix} \bar{\mathbf{p}}_n \\ v_n \\ \phi_n \end{bmatrix} = \underbrace{\begin{bmatrix} \bar{\mathbf{p}}_{n-1} + \tilde{\mathbf{e}}(\phi_{n-1})v_{n-1}\Delta t_{\mathrm{t},n} \\ v_{n-1} \\ \phi_{n-1} \end{bmatrix}}_{\mathbf{f}_\mathrm{l}(\mathbf{x}_{n-1},\mathbf{u}_n)} + \underbrace{\begin{bmatrix} \boldsymbol{\delta}\bar{\mathbf{p}}_n \\ \delta v_n \\ \delta\phi_n \end{bmatrix}}_{\mathbf{w}_{\mathrm{l},n}},$$

with vehicle x-vector $\tilde{\mathbf{e}}_\mathrm{x}(\phi) = \begin{bmatrix}\cos(\phi) & \sin(\phi)\end{bmatrix}^\mathrm{T}$, position variation $\boldsymbol{\delta}\bar{\mathbf{p}}_n$ as defined above, scalar velocity and angle variations $\delta v_n$ and $\delta\phi_n$, respectively. Since we assume that $\delta\phi_n \ll 1$, i.e. only a slow change in angle w.r.t. the motion forward and backward, we can model variation as

$$\mathbf{w}_{\mathrm{l},n} \sim \mathcal{N}(\mathbf{0}, \mathbf{Q}_{\mathrm{l},n}) \qquad \mathbf{Q}_{\mathrm{l},n} = \begin{bmatrix} \mathbf{Q}_{\mathrm{pv},n} & \mathbf{0} \\ \mathbf{0} & \Delta t_{\mathrm{t},n}\sigma_\phi^2 \end{bmatrix}$$
$$\mathbf{Q}_{\mathrm{pv},n} = \begin{bmatrix} \frac{1}{3}c_\phi^2\Delta t_{\mathrm{t},n}^3 & \frac{1}{3}s_\phi c_\phi \Delta t_{\mathrm{t},n}^3 & \frac{1}{2}c_\phi\Delta t_{\mathrm{t},n}^2 \\ \frac{1}{3}s_\phi c_\phi\Delta t_{\mathrm{t},n}^3 & \frac{1}{3}s_\phi^2\Delta t_{\mathrm{t},n}^3 & \frac{1}{2}s_\phi\Delta t_{\mathrm{t},n}^2 \\ \frac{1}{2}c_\phi\Delta t_{\mathrm{t},n}^2 & \frac{1}{2}s_\phi\Delta t_{\mathrm{t},n}^2 & \Delta t_{\mathrm{t},n} \end{bmatrix}\sigma_\mathrm{v}^2,$$

where we use the shorthand notation

$$c_\phi \equiv \cos(\phi_{n-1}) \qquad s_\phi \equiv \sin(\phi_{n-1}).$$

### *E. Observation*

Since we have used the actual ToA measurements already as system input, the observation model relates positions and (predicted) trx times as

$$z_{\mathrm{m},n} = \overbrace{t_n^{k_\mathrm{t}} + \delta t_\mathrm{a}^{k_\mathrm{t}} - t_n^{k_\mathrm{r}} + \tfrac{1}{c}\sqrt{\left(\mathbf{p}_n^{k_\mathrm{r}} - \mathbf{p}_n^{k_\mathrm{t}}\right)^\mathrm{T}\left(\mathbf{p}_n^{k_\mathrm{r}} - \mathbf{p}_n^{k_\mathrm{t}}\right)}}^{h_\mathrm{m}(\mathbf{x}_n)} + \underbrace{\delta t_{\mathrm{m},n}}_{w_{\mathrm{m},n}} = 0$$

with speed of light $c$, and UWB rx time measurement noise $w_{\mathrm{m},n} \sim \mathcal{N}(0, \sigma_\mathrm{m}^2)$ with variance $\sigma_\mathrm{m}^2$. The tx antenna delay $\delta t_\mathrm{a}^k$, is the elapsed time between timestamping the tx packet and the actual tx. It is a hardware parameter individual to each unit that can also be used as a state variable for calibration.

For stability reasons—estimation of the mean clock skew $\frac{1}{K}\sum_{k=1}^K \tau_n^k$ is ill-conditioned—we (loosely) link the current transmit time to system time $t_{\mathrm{s},n}$ at the time of packet arrival at the measurement PC, which gives us another equation

$$\underbrace{t_{\mathrm{s},n}}_{z_{\mathrm{s},n}} = \underbrace{t_n^{k_\mathrm{t}}}_{h_\mathrm{s}(\mathbf{x}_n)} + \underbrace{\delta t_\mathrm{s}}_{w_{\mathrm{s},n}}$$

with system time error $w_{\mathrm{s},n} \sim \mathcal{N}(0, \sigma_\mathrm{s}^2)$ with variance $\sigma_\mathrm{s}^2$.

### *F. Extended Kalman filter*

Using the input $\mathbf{u}_n$, state $\mathbf{x}_n$, and system models as defined above, our algorithm is based on a standard EKF formulation. The predicted and updated states $\mathbf{x}_{n|n-1}$ and $\mathbf{x}_{n|n}$ in step $n$ are normally distributed

$$\mathbf{x}_{n|n-1} \sim \mathcal{N}\left(\boldsymbol{\mu}_{n|n-1}, \boldsymbol{\Sigma}_{n|n-1}\right) \quad \mathbf{x}_{n|n} \sim \mathcal{N}\left(\boldsymbol{\mu}_{n|n}, \boldsymbol{\Sigma}_{n|n}\right)$$

with means $\boldsymbol{\mu}$ and covariance matrices $\boldsymbol{\Sigma}$.

In the prediction step of the filter, we compute

$$\boldsymbol{\mu}_{n|n-1} = \mathbf{f}(\boldsymbol{\mu}_{n-1|n-1}, \mathbf{u}_n)$$
$$\boldsymbol{\Sigma}_{n|n-1} = \mathbf{F}_n\boldsymbol{\Sigma}_{n-1|n-1}\mathbf{F}_n^\mathrm{T} + \mathbf{Q}_n \quad \mathbf{F}_n = \frac{\mathbf{f}}{\mathrm{d}\mathbf{x}^\mathrm{T}}\Big|_{\boldsymbol{\mu}_{n-1|n-1},\mathbf{u}_n}$$

In C1 and C2, transition $\mathbf{f}$ and covariances $\mathbf{Q}$ are

$$\mathbf{f} = \begin{bmatrix}\mathbf{f}_\mathrm{s}^{k\in\mathcal{K}_\mathrm{A}} & \mathbf{f}^{k\in\mathcal{K}_\mathrm{T}}\end{bmatrix}^\mathrm{T} \qquad \mathbf{f}^{k\in\mathcal{K}_\mathrm{T}} = \begin{bmatrix}\mathbf{f}_\mathrm{s}^k & \mathbf{f}_\mathrm{l}^k\end{bmatrix}^\mathrm{T}$$
$$\mathbf{Q}_n = \mathrm{diag}\{\mathbf{Q}_{\mathrm{s},n}^{k\in\mathcal{K}_\mathrm{A}}, \mathbf{Q}_n^{k\in\mathcal{K}_\mathrm{T}}\} \quad \mathbf{Q}_n^{k\in\mathcal{K}_\mathrm{T}} = \mathrm{diag}\{\mathbf{Q}_{\mathrm{s},n}^k, \mathbf{Q}_{\mathrm{l},n}^k\},$$

where $\mathrm{diag}\{\cdot\}$ denotes the block diagonal matrix and $\mathbf{Q}_n^{k\neq\{k_\mathrm{t},k_\mathrm{r}\}} = \mathbf{0}$. In C3 and C4 we have

$$\mathbf{f} = \begin{bmatrix}\mathbf{f}_\mathrm{l} & \mathbf{f}_\mathrm{s}^{k\in\mathcal{K}}\end{bmatrix}^\mathrm{T} \qquad \mathbf{Q}_n = \mathrm{diag}\{\mathbf{Q}_{\mathrm{l},n}, \mathbf{Q}_{\mathrm{s},n}^{k\in\mathcal{K}}\}.$$

In the update step, the innovation $\mathbf{y}_n$, its covariance $\mathbf{S}_n$, and Kalman gain $\mathbf{K}_n$ are

$$\mathbf{y}_n \equiv \begin{bmatrix} y_\mathrm{m} \\ y_\mathrm{s} \end{bmatrix} = \underbrace{\begin{bmatrix} z_{\mathrm{m},n} \\ z_{\mathrm{s},n} \end{bmatrix}}_{\mathbf{z}_n} - \underbrace{\begin{bmatrix} h_\mathrm{m}(\boldsymbol{\mu}_{n|n-1}) \\ h_\mathrm{s}(\boldsymbol{\mu}_{n|n-1}) \end{bmatrix}}_{\mathbf{h}(\boldsymbol{\mu}_{n|n-1})}$$
$$\mathbf{S}_n \equiv \begin{bmatrix} s_\mathrm{mm} & s_\mathrm{ms} \\ s_\mathrm{ms} & s_\mathrm{ss} \end{bmatrix} = \mathbf{H}_n\boldsymbol{\Sigma}_{n|n-1}\mathbf{H}_n^\mathrm{T} + \mathbf{R}_n$$
$$\mathbf{K}_n = \boldsymbol{\Sigma}_{n|n-1}\mathbf{H}_n^\mathrm{T}\mathbf{S}_n^{-1}$$

and the state update becomes

$$\boldsymbol{\mu}_{n|n} = \boldsymbol{\mu}_{n|n-1} + \mathbf{K}_n\mathbf{y}_n$$
$$\boldsymbol{\Sigma}_{n|n} = \left(\mathbf{I} - \mathbf{K}_n\mathbf{H}_n\right)\boldsymbol{\Sigma}_{n|n-1},$$

where

$$\mathbf{H}_n = \frac{\mathrm{d}\mathbf{h}}{\mathrm{d}\mathbf{x}^\mathrm{T}}\bigg|_{\boldsymbol{\mu}_{n|n-1}} \qquad \mathbf{R}_n = \mathrm{diag}\{\sigma_\mathrm{m}^2, \sigma_\mathrm{s}^2\}.$$

For outlier elimination, we reject packets with Mahalanobis distance above a threshold, i.e. that do not meet $\frac{y_\mathrm{m}^2}{s_\mathrm{mm}} \leq \delta\breve{y}_\mathrm{max}^2$.

For evaluation in Section IV, we use the parameters

$$\sigma_\tau^2 = 10\,\tfrac{\mu\mathrm{s}^2}{\mathrm{s}^2\cdot\mathrm{s}} \quad \sigma_\mathrm{v}^2 = 0.01\,\tfrac{\mathrm{m}^2}{\mathrm{s}^2\cdot\mathrm{s}} \quad \sigma_\phi^2 = 10.0\,\tfrac{\mathrm{mrad}^2}{\mathrm{s}^2\cdot\mathrm{s}}$$
$$\sigma_\mathrm{m}^2 = 0.04\,\tfrac{\mathrm{ns}^2}{\mathrm{s}} \quad \sigma_\mathrm{s}^2 = 0.01\,\tfrac{\mathrm{Ms}^2}{\mathrm{s}} \quad \delta\breve{y}_\mathrm{max}^2 = 8.0.$$

## IV. Experimental results

We performed a measurement with the vehicle starting from the ramp and moving in positive x-direction. It stopped at 10 positions between 3 and 36 m to evaluate error statistics, ground truth was taken from lidar data. The algorithm was applied on recorded raw data in configurations C1–C4 to ensure identical conditions. In C1 and C2, where individual tag positions are computed, the vehicle pose was estimated in post-processing by least squares fit to the tag location estimates.

Fig. 5 shows evaluation results for C1–C4 from top to bottom. As a qualitative conclusion, estimates are similar for all configurations close to the loading dock, and degrade as the vehicle moves away. This is a consequence of lower accuracy measurements due to reduced signal power as well as geometric dilution of precision. In C1, for large x-values, tag position estimates completely diverge. Hence, there is no meaningful estimate of vehicle position possible, which shows as an arbitrarily rotating vehicle outline in the top right corner. Quantitative statistical results for the pose estimation errors in position $\delta x$, $\delta y$, and angle $\delta\phi$ that confirm these observations are shown in Fig 6. More specifically, in the best configuration C4, the median error $\delta x$ stays below 19 cm, with an inter-quantile-range (IQR) below 12 cm. The median error $\delta y$ grows from about 5 cm to a little under 1 m, with IQR under 6 cm, and the angle error $\delta\phi$ varies in median between $-4.7°$ and $2.4°$ with a maximum IQR of $1.0°$.

We conclude that adding measurements and geometric constraints from C1 to C4 improves the results considerably. Even though the only difference between C1 and C2 is that packets exchanged between mobile tags are also used, this leads to more closely related individual tag position estimates. By including these packets (that generally have good connectivity), the ranges—and hence the relative positions—are implicitly calculated. Also, there are additional measurements available for tag synchronization, which leads to overall improvement. Mounting the tags on a rigid body whose pose is estimated in C3 leads to completely coordinated tag motions, even more than in C2. Errors seen in C1 such as diverging individual tag estimates are completely eliminated. As the vehicle x-coordinate increases, accuracy and precision in y-direction generally decrease more than in x, which is expected given the geometric arrangement of the anchors in a ToA-based setup. Therefore, restricting sideways motion of the vehicle in C4 greatly improves the results mainly in y-direction.

Remaining errors may have different sources that cannot be entirely quantified. Tags are directly mounted on a metallic container with ribs for reinforcement (cf. Fig. 3) that act as many potential points for RF signal reflections, thus leading to multipath propagation. Furthermore, we formulated a plane estimation problem, which is not strictly fulfilled. Uneven road surface and the possibility of the vehicle container to shift in height by some centimeters are most problematic when the vehicle is close to the anchors. Uncertainties in anchor position measurement as well as in ground truth assessment by the lidar sensor also add to evaluation error.

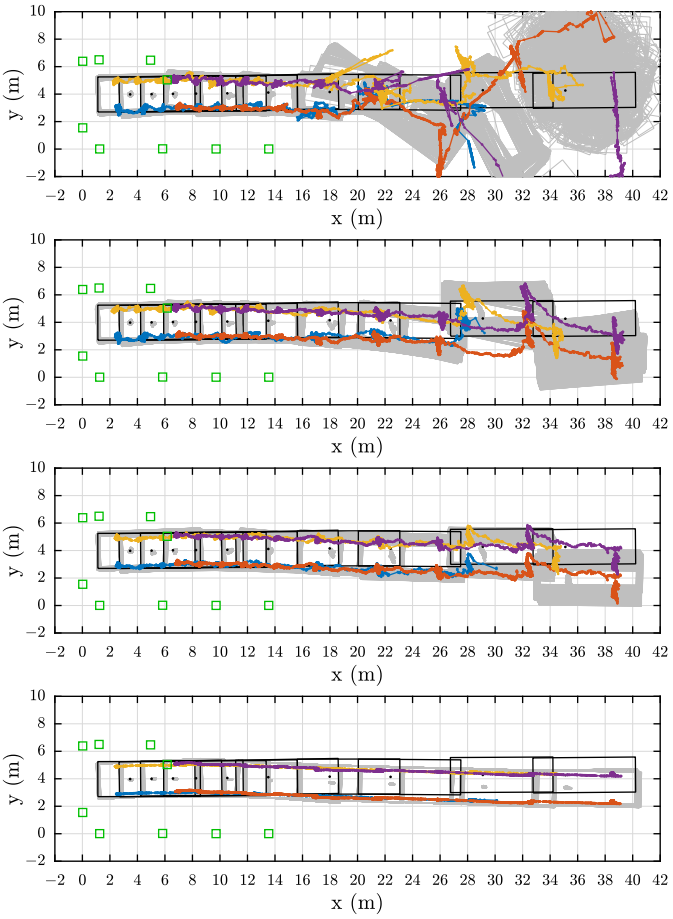


Fig. 5. Top view of evaluation results in C1 (top) to C4 (bottom). Anchor positions are marked with green squares. Colored lines show tag position estimates from which vehicle poses are derived. Estimated vehicle (container) outlines and vehicle origin positions are shown as gray rectangles and dots, respectively. Black rectangles and dots indicate lidar ground truth.

## V. Conclusions

We have introduced an UWB localization system used for operations at a logistics hub and shown its applicability in a real-world measurement scenario. An EKF-based algorithm for simultaneous localization and synchronization using broadcast packets was presented. Its unique features are the use of time differences between consecutive packets as system input, which allows for a simple unscheduled messaging protocol, and the incorporation of geometric constraints, which has been shown to significantly improve results. Even at a distance of more than 20 m from the nearest anchor in an unfavorable geometric constellation, the vehicle pose estimate in the best configuration shows good agreement with the ground truth.

## Acknowledgments

This work has received funding from the European Union's Horizon 2020 research and innovation programme under grant agreement No 101006817. It has been supported by the LCM – K2 Center within the framework of the Austrian COMET-K2 program.

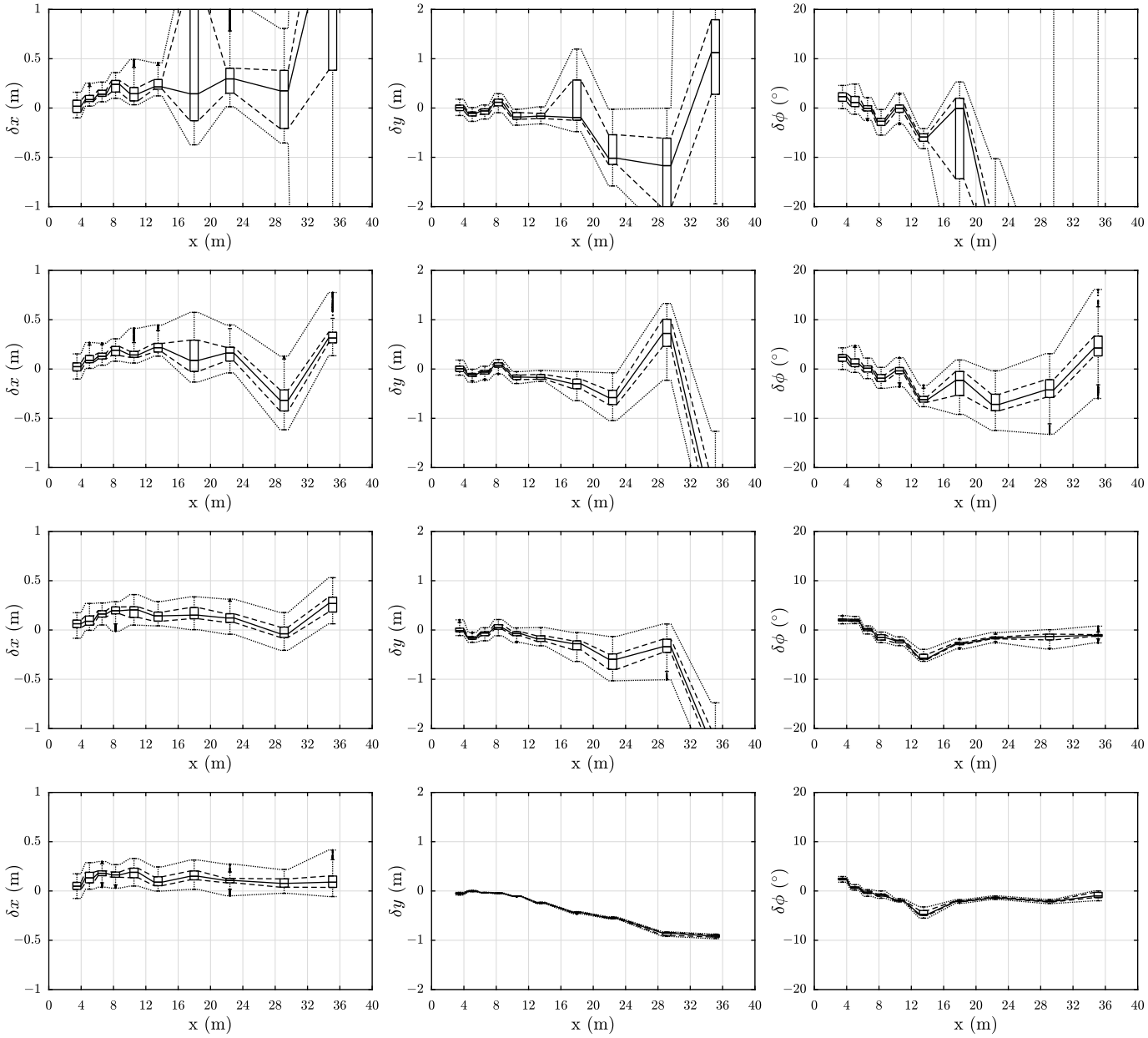


Fig. 6. Statistics of estimation error $\delta x$, $\delta y$, and $\delta\phi$ (left to right) in configuration C1–C4 (top to bottom) for the 10 static positions along the x-axis between 3.47 and 35.11 m. Median value is plotted as solid, 25 % and 75 %-quantiles as dashed, and minimum/maximum values as dotted lines.

## REFERENCES


[1] *AWARD: All Weather Autonomous Real logistics operations and Demonstrations*. Accessed: Dec. 4, 2023. [Online]. Available: https://award-h2020.eu/.

[2] S. Gezici and H. V. Poor, "Position estimation via ultra-wide-band signals," *Proc. IEEE*, vol. 97, no. 2, pp. 386–403, Feb. 2009.

[3] A. Alarifi et al., "Ultra wideband indoor positioning technologies: Analysis and recent advances," *Sensors*, vol. 16, no. 5, 2016.

[4] J. Zheng and Y.-C. Wu, "Joint time synchronization and localization of an unknown node in wireless sensor networks," *IEEE Trans. Signal Process.*, vol. 58, no. 3, pp. 1309—1320, Mar. 2010.

[5] R. M. Vaghefi and R. M. Buehrer, "Cooperative joint synchronization and localization in wireless sensor networks," *IEEE Trans. Signal Process.*, vol. 63, no. 14, pp. 3615—3627, July 2015.

[6] B. Etzlinger, F. Meyer, F. Hlawatsch, A. Springer and H. Wymeersch, "Cooperative Simultaneous Localization and Synchronization in Mobile Agent Networks," in *IEEE Trans. Signal Process.*, vol. 65, no. 14, pp. 3587–3602, July 2017.

[7] S. Zhao, X.-P. Zhang, X. Cui and M. Lu, "A New TOA Localization and Synchronization System With Virtually Synchronized Periodic Asymmetric Ranging Network," in *IEEE Internet of Things Journal*, vol. 8, no. 11, pp. 9030–9044, June 2021.

[8] S. Thrun, W. Burgard and D. Fox, *Probabilistic Robotics*. The MIT Press, 2005.

[9] Qorvo, Inc., *DW1000 3.5 - 6.5 GHz Ultra-Wideband (UWB) Transceiver IC with 1 Antenna Port*. Accessed: Dec. 4, 2023. [Online]. Available: https://www.qorvo.com/products/p/DW1000.

[10] SLAMTEC Co., Ltd., *RPLIDAR C1*. Accessed: Dec. 4, 2023 [Online]. Available: https://www.slamtec.com/en/C1/.